Electroluminescence in Unipolar-Doped $In_{0.53}Ga_{0.47}As$/AlAs Resonant-Tunneling Diodes: A Competition between Interband Tunneling and Impact Ionization

E. R. Brown,[1, a)] W-D. Zhang,[1] T.A. Growden,[2] P. Fakhimi,[3] and P.R. Berger[3]

[1]*Department of Physics, Wright State University, 3640 Colonel Glenn Hwy, Dayton, OH 45435, USA*
[2]*U.S. Naval Research Laboratory, Washington, DC 20375, USA*
[3]*Department of Electrical and Computer Engineering, Ohio State University, Columbus, OH 43210, USA*

a) email: elliott.brown@wright.edu Phone: (937) 344-9712

ABSTRACT

We measure and analyze the light emission from a room-temperature, n-type unipolar-doped $In_{0.53}Ga_{0.47}As$/AlAs double-barrier resonant-tunneling diode (RTD) that occurs just above the $In_{0.53}Ga_{0.47}As$ band-edge and peaks around 1631 nm. The emission is attributed to electron-hole recombination emission made possible by holes generated in the high-field region on the collector side of the device by interband tunneling and impact ionization, which contribute comparable hole densities according to our analysis. Although the external quantum efficiency (EQE) in our experimental configuration is rather low ($\approx 2\times10^{-5}$ at 3.0-V bias), limited by sub-optimal output coupling, the internal quantum efficiency (IQE) is much higher ($\approx$6% at 3.0 V bias) as derived from the experimental EQE and a radiometric analysis. To check this value and better understand the transport physics, we also carry out an independent estimate of the IQE using a combined interband-tunneling impact-ionization transport model, which yields IQE $\approx$10% at 3.0 V bias. The satisfactory agreement of theory with experimental data suggests that an RTD designed for better hole transport and a superior optical coupling could become a useful light emitting device while retaining the intrinsic functionality of high-speed negative differential resistance (NDR), and all without the need for resistive p-type doping.

[a)] Electronic mail: elliott.brown@wright.edu

I. INTRODUCTION

Interband tunneling has been an important aspect of electron transport in crystalline solids since the seminal paper by Zener in 1934.[1] However, the useful demonstration in electronic devices had to wait for the development of semiconductor technology in the early 1950s with the demonstration of controllable "breakdown" in back-biased Ge p-n Zener diodes. And then in the same decade, the interband tunneling effect was accentuated to make the first device with negative differential resistance at room temperature – the Esaki tunnel diode[2] – which ultimately led to the Physics Nobel Prize in 1973. More recently, interband tunneling has been revived with lateral tunneling field effect transistors (TFETs) as a means of overcoming the fundamental lower limit (60 mV/decade) of turn-on voltage in Si MOS devices.[3,4,5,6] And it has also been utilized to make highly sensitive radio-frequency rectifiers in p-n doped, Type-III (broken-gap), III-V heterostructures,[7] and highly efficient tandem heterojunction solar cells.[8] The primary purpose of this paper is to demonstrate that interband tunneling may also be useful for n-type unipolar-doped photonic sources via electroluminescence at room temperature. Double-barrier RTDs have already proven their utility as room-temperature optical detectors in optoelectronic integrated circuits,[9] but not yet as practical photonic sources. A key issue is their internal quantum efficiency (IQE).

A secondary purpose of this paper is to propose that the holes created on the collector side by interband tunneling or impact ionization can transfer efficiently to the emitter side by *intraband* tunneling through a straddling-gap (Type-I-offset) double-barrier structure. In the present case, the structure is a garden-variety $In_{0.53}Ga_{0.47}As$/AlAs double-barrier RTD of the type normally used for high-speed electron resonant tunneling devices. Hole resonant tunneling is known to occur in such RTD structures when they are doped p-type,[10] but is significantly more complicated than electron resonant tunneling because of light-hole, heavy-hole mixing effects. However, we emphasize that the resonant tunneling of holes is not required for the IQE results presented here; rather, just significantly high overall hole transmission probability. Hence our results suggest that both electron and hole intraband tunneling are occurring simultaneously and efficiently through the same double-barrier structure. And more importantly, both tunneling mechanisms are strong enough to enable a light emission mechanism that is surprisingly efficient considering there is no p-type doping in the structure.

We have already observed room-temperature electroluminescence from n-type, unipolar GaN/AlN[11] and $In_{0.53}Ga_{0.47}As$[12] double-barrier RTDs via emission from the sidewalls of mesa-isolated devices. Both were attributed qualitatively to hole generation by interband tunneling in the device structure, although proof was lacking because of unknown quantum efficiencies and the lack of a comparison with the other possible source of holes – impact ionization. Here we report on band-edge emission from a separate unipolar $In_{0.53}Ga_{0.47}As$/AlAs RTD designed for partial vertical emission, and thus take the analysis

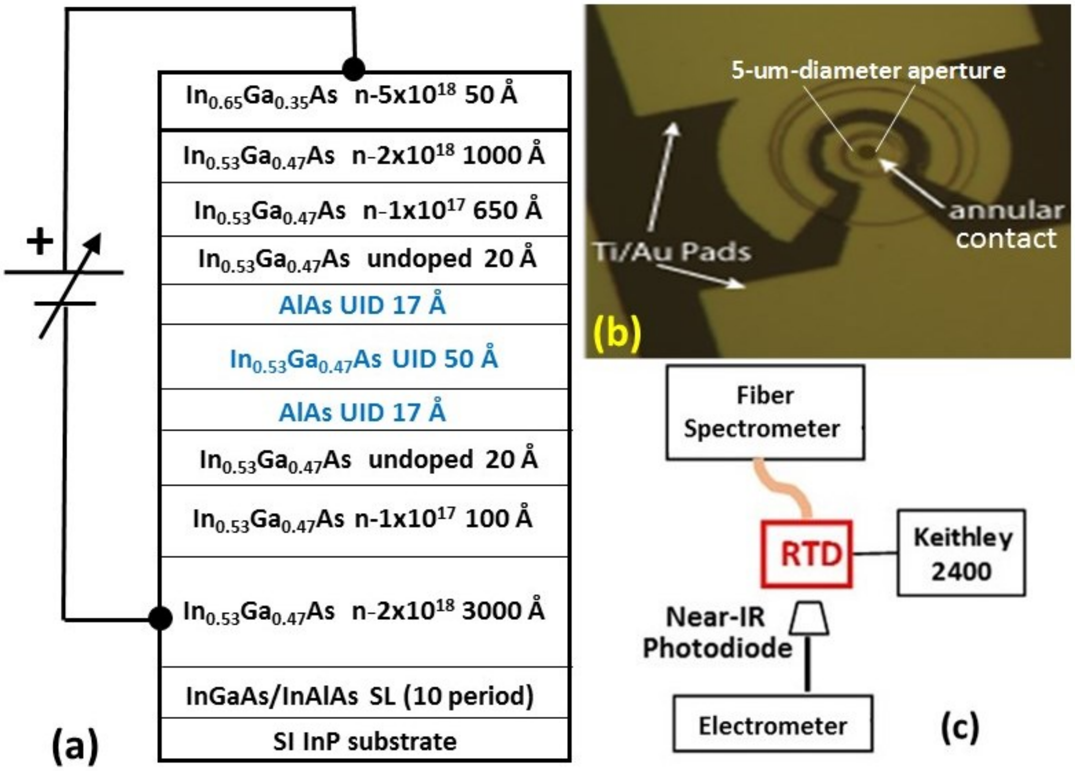

FIG. 1. (a) MBE-growth stack. (b) Microphotograph of fabricated device with vertical emission aperture. (c) Experimental set-up for measurement of electrical and optical characteristics.

an important step further by deriving the IQE from experimental measurements and calculations using two independent methods. The first method is based on a direct measurement of the experimental external quantum efficiency (EQE) and a radiometric calculation of the optical coupling factor. The second is based on a holistic charge-transport computation of the available hole current by both interband tunneling and impact ionization on the collector side, and radiative recombination on both sides. Interband tunneling and impact ionization are shown to yield comparable available hole currents with impact ionization exceeding interband tunneling at modest bias (around the peak voltage of the RTD) and interband tunneling dominating at the highest bias tested where the strongest and most efficient light emission occurs.

II. DEVICE DESIGN AND EXPERIMENTAL CHARACTERIZATION

The device demonstrated here is a “garden-variety” $In_{0.53}Ga_{0.47}As$ RTD, designed for electrical-NDR, and grown by molecular-beam epitaxy on a semi-insulating InP substrate and having the growth stack and n-type doping profile as shown in Fig. 1(a). It is similar in design to the state-of-the-art in RTDs that have in recent years extended the maximum frequency of solid-state self-oscillators above 1.0 THz,[13] continuing to advance RTDs as the fastest room-temperature solid-state oscillators since 1991.[14] The active region is comprised of two unintentionally doped (UID) AlAs barriers (thickness ≈ 1.7 nm, or 6 monolayers) separated by an undoped $In_{0.53}Ga_{0.47}As$ quantum-well (width = 5.0 nm) layer, such that an electron quasibound level, $U_{1,e}$, occurs in the quantum well at an energy level of ≈0.193 eV above the $In_{0.53}Ga_{0.47}As$ conduction band edge at zero bias. Immediately outside the double-barrier structure are 2-nm undoped spacer layers, and then low n-doped ($N_d = 1\times10^{17}$ cm^{-3}) layers having thicknesses of 65 and 10 nm on the top and bottom sides, respectively. Outside of the n-doped regions are n$^+$-doped ($N_d = 2\times10^{18}$ cm^{-3}) contact layers to which electrical ohmic contacts are made. The structure is designed for positive bias on the top (collector) side, which tends to deplete the top 65-nm n-type region and create a low collector-side capacitance for high-speed device operation in oscillators and switches. And because of the large confinement energy, $U_{1,e}$, a relatively high bias voltage of $V_B \sim 2.0$ V is required to achieve the peak condition of resonant (intraband) tunneling. As described below, the large bias and depleted collector layer are important factors in promoting the cross-gap electroluminescence.

Working devices were fabricated as 15-μm-diam circular vertical mesas including a top annular ohmic contact with a 5-μm-diam pinhole in the center to couple out light vertically for accurate free-space power measurements. A microphotograph of the fabricated annular-contact structure is shown in Fig. 1(b). For device characterization, the set-up shown in Fig. 1(c) was used, consisting of a precision I-V probe station, a near-IR calibrated photo detector, and a near-IR overmoded-fiber spectrometer. The ambient temperature was T≈300 K. The detector was a large-area (3-mm diameter) Ge photodiode with spectral response between 800 and 1800 nm and having a peak responsivity of $\Re \approx 0.85$ A/W at a wavelength of 1550 nm. It was optically coupled through free-space with the photodiode located as close-as-practical (≈3 mm, limited by packaging issues) to the DBRTD. Its output was dc coupled to a solid-state electrometer having a current noise floor of ~1 pA. The fiber spectrometer was a room-temperature near-infrared (NIR) InGaAs-array-grating instrument sensitive between 880 and 1750 nm and having a programmable spectral resolution,[15] chosen for the present experiments to be 0.5 nm.

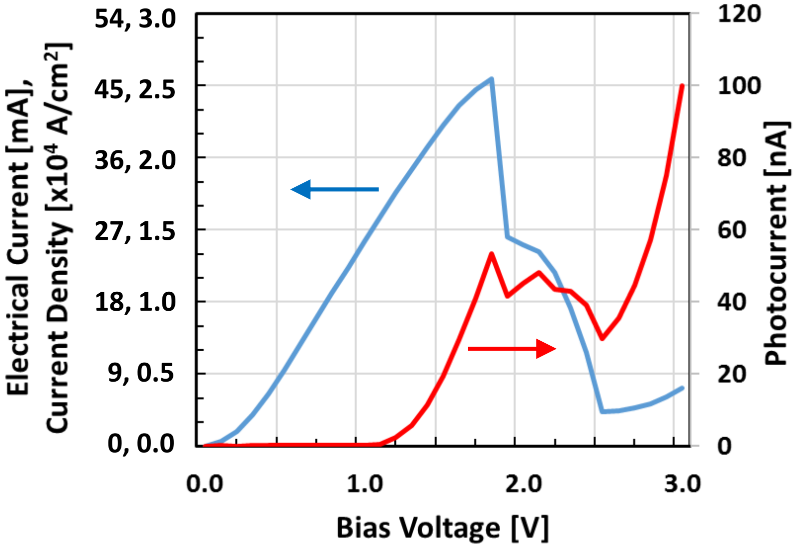

FIG. 2. Experimental I-V curve (left vertical axis) and L-V curve (right vertical axis) at 300 K.

Shown in Fig. 2 is the electrical current-voltage (I-V) and current-density curves (left vertical axis) along with the broadband light-vs-voltage (L-V) curve measured for the device (right vertical axis), where L is the photodiode output current measured in units of nA. The I-V curve displays a pronounced electrical NDR region having a peak voltage of 1.8 V, a valley voltage of 2.5 V, and a current peak-to-valley current ratio (PVCR) of 10.7, which is typical for high-quality $In_{0.53}Ga_{0.47}As$ RTDs at room temperature. The terminal electric current density, J_E, is calculated from the current through division by the mesa area of 177 um^2, which yields a peak current density, J_E, of ≈26 kA/cm^2. In the NDR region, between the peak and valley, there is a chair-like structure usually indicative of instability, or self-oscillations driven by the modestly large current density here, and we made no attempt to terminate the RTD with low enough source impedance to suppress oscillations in the present experiments. The L-V curve, displays a threshold of light emission at ≈1.2 V, followed by a rapid increase to a local maximum at the peak voltage of the I-V curve. In the NDR region, the L-V curve is jagged suggesting that the light emission is affected by the electrical instability and therefore likely occurring in the active region of the RTD. Above the valley voltage the light emission increased very rapidly again, reaching a maximum (for the present experiments) at 3.0 V. The L-V curve in this region increases with bias voltage faster than the electrical current, which is an important clue in the interpretation provided by our model for the electroluminescence, described below.

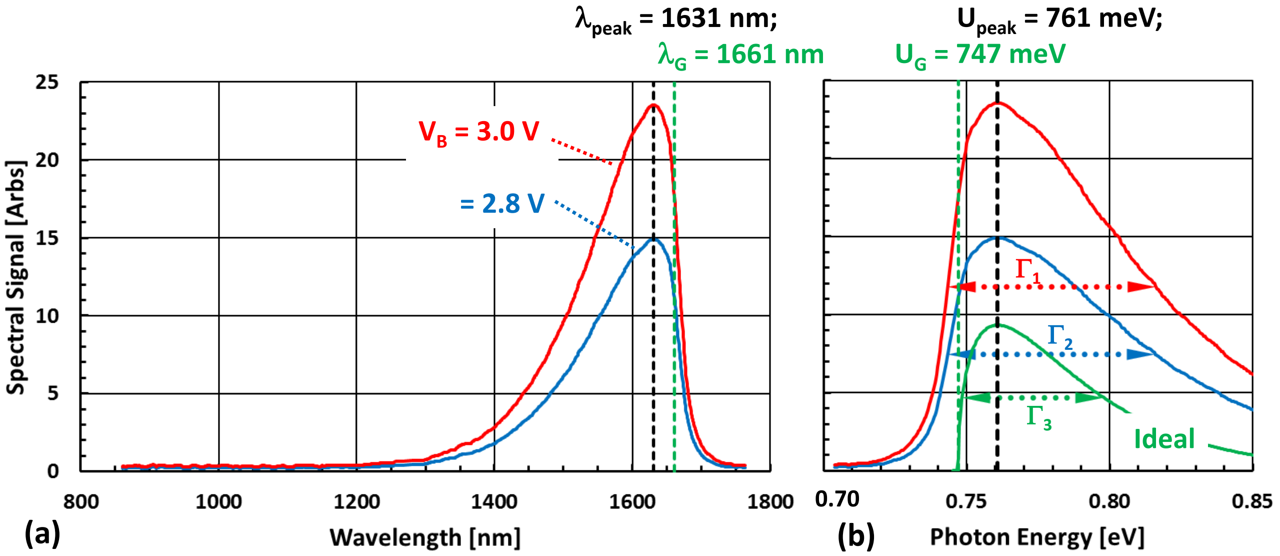

FIG. 3. (a) Experimental light-emission spectra at 300 K plotted vs wavelength for two bias voltages (2.8 and 3.0 V). The peak of both spectra occurs at ≈1631 nm, and the full-width at half-maximum is ≈148 nm. (b) Same light spectra as in (a) but plotted vs photon energy, including the "ideal" spectrum (offset for clarity and plotted in green) for $In_{0.53}Ga_{0.47}As$ as a direct-bandgap semiconductor.

The emission spectra are plotted in Fig. 3(a) (vs. wavelength) and 3(b) (vs. photon energy) at V_B = 2.8 and 3.0 V, both above the RTD valley voltage. V_B = 3.0 V yielded the strongest and most efficient electroluminescence performance characteristics measured on this device. For both bias voltages, the long wavelength emission edge is at λ ≈ 1680 nm — just beyond the $In_{0.53}Ga_{0.47}As$ bandgap wavelength of 1661 nm (corresponding to $U_G \approx 0.747$ eV at 300 K [Ref. 16]). However, the peaks for both emission spectra occur at λ ≈ 1631 nm ($h\nu = hc/\lambda = 0.761$ eV, where c is the speed of light), so are slightly *blue-shifted* by ≈14 meV relative to the band edge. This shift is well known from the following "ideal" cross-gap spectral intensity applicable to a bulk, direct-bandgap semiconductor:[17]

$$S(\nu) = H\cdot(h\nu - U_G)^{1/2}\cdot\exp[-(h\nu - U_G)/k_BT)], \tag{1}$$

where H is a frequency-independent constant, no cavity effects are assumed, and k_B and h are the Boltzmann and Planck constants, respectively. Eqn. (1) predicts a peak shift of $(1/2)\cdot k_BT = 12.9$ meV relative to U_G – close to our experimental shift of 14 meV. As plotted in Fig. 3(b), the experimental spectral peaks align with the ideal one to within 1 meV, which is the approximate uncertainty in photon energy around λ = 1650 nm associated with the fiber spectrometer.

In spite of the good peak agreement, there is significantly more radiation from the device than the ideal spectrum at wavelengths below the peak, as well as sub-bandgap radiation at wavelengths beyond the peak. As shown in Fig. 3(b), these both broaden the experimental emission to a FWHM of Γ_1 = 72 meV

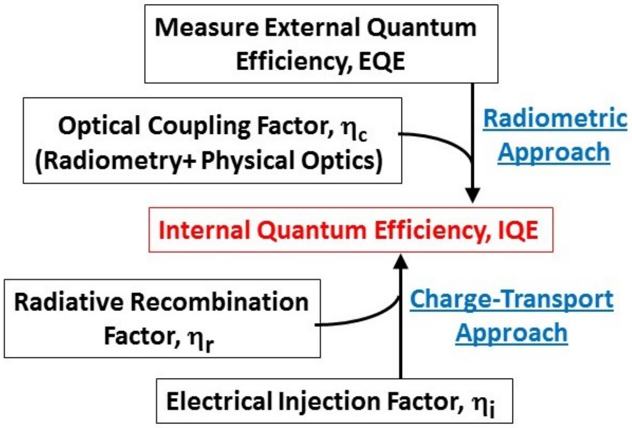

FIG. 4. Methodology for estimating the IQE by two separate approaches.

at $V_B = 3.0$ V ($\Delta\lambda = 148$ nm), and $\Gamma_2 = 71$ meV at $V_B = 2.8$ V. These are to be compared to $\Gamma_3 = 46.5$ meV for the ideal spectrum at T = 300 K (i.e., $\Gamma_3 = 1.8 \cdot k_B T$). A likely reason for this discrepancy is alloy broadening – a mechanism caused by random distribution of the atoms in a ternary alloy such as $In_{0.53}Ga_{0.47}As$ [Ref. 17]. However, aside from the broadening effect, there was no other experimental evidence for significant non-ideal emission in the range between 850 and 1750 nm. In fact, our FWHM is comparable to that of commercial, 300-K p-n LEDs with peak emission between 1600 and 1650 nm, which is typically between $\Delta\lambda = 130$ and 150 nm.[18]

III. QUANTUM EFFICIENCIES

III.A. Experimental EQE and Radiometric Estimation of IQE

Knowing experimentally that the majority of emission is occurring within the spectral range of the wideband photodiode of Fig. 1(c), we can proceed immediately with estimates of the light emission figures-of-merit: the external and internal quantum efficiencies (EQE and IQE). We follow the methodology outlined in Fig. 4 by first measuring the EQE. For this, we positioned the photodiode ≈3.0 mm above the RTD pinhole and separately measured its optical responsivity to be $\Re \approx 0.85$ A/W at $\lambda = 1550$ nm. For a Ge photodiode ($U_G = 0.66$ eV; $\lambda_G = 1.88$ μm; both at 300 K) this responsivity should be approximately flat with wavelength over the ~148-nm-FWHM, 1631-nm-centered emission spectra of Fig. 3(a). The set-up-dependent EQE was then estimated from the expression

$$\mathrm{EQE} \approx e \cdot I_{ph} / (\Re \cdot I_E \cdot h\nu) \tag{2}$$

where I_{ph} is the photodiode dc current and I_E is the terminal RTD electrical current, measured at each bias voltage of Fig. 2. The plot of EQE is shown in Fig. 5 (left vertical axis) where we see a very rapid rise with V_B, but a maximum value (at V_B= 3.0 V) of only $\approx 2 \times 10^{-5}$. To extract the IQE we use the expression

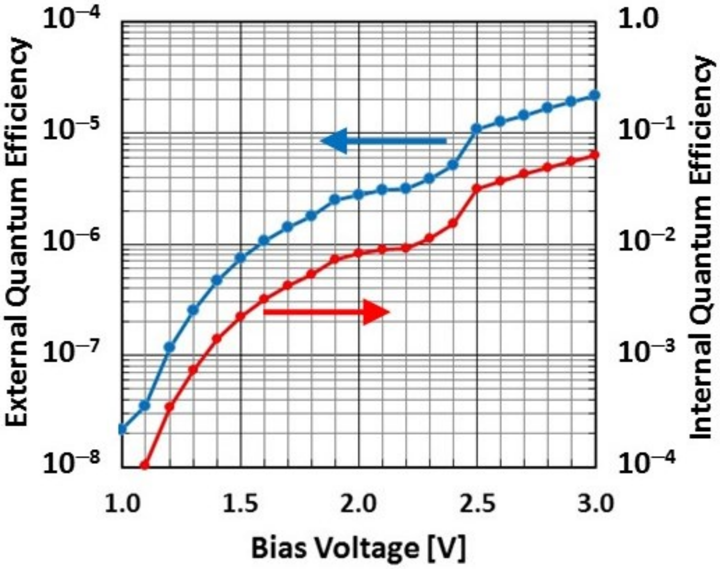

FIG. 5. External quantum efficiency (EQE) obtained directly from experiments (left vertical axis). Internal quantum efficiency calculated using the radiometric approach of Fig. 4 (right vertical axis).

$$\mathrm{EQE} = \eta_c \cdot \mathrm{IQE} \qquad (3)$$

where η_c is the optical-coupling factor [Ref. 17].

To obtain an estimate of the radiometric IQE, we performed a separate calculation of η_c using radiometric methods and physical optics.[19] We treated the light emission from the pinhole as Lambertian, consistent with the emission from common LEDs. This includes the following effects, in decreasing order of importance: (1) the fraction of Lambertian radiation from the pinhole collected by the photodiode; (2) the refractive-index mismatch between $In_{0.53}Ga_{0.47}As$ ($n \approx 3.4$ at 1550 nm) and air; (3) the reduction in external-to-internal radiative power associated with the pinhole-to-RTD area ratio; and (4) the polarization-dependent transmittance between $In_{0.53}Ga_{0.47}As$ and air, averaged over angle between $\theta = 0$ and the angle of total-internal-reflection ($\theta \approx 17^{\circ}$). The net result is $\eta_c \approx 3.4\times10^{-4}$. This might seem small, but one must remember that in the present mesa-isolated device a large fraction of the radiation propagates either through the mesa sidewalls, or into the InP substrate where it is trapped by total internal reflection or transmitted out the chip sidewalls. Lacking the half-ball lens coupling and parabolic mirrors or external reflecting "cups" as commonly used in efficient LEDs, the vast majority of internal radiation is practically unobservable in our experiments. Given this value of η_c we obtain the curve of IQE plotted in Fig. 5 (right vertical axis). The maximum value of IQE (again at $V_B = 3.0$ V) is ≈ 6%, as announced last year.[20]

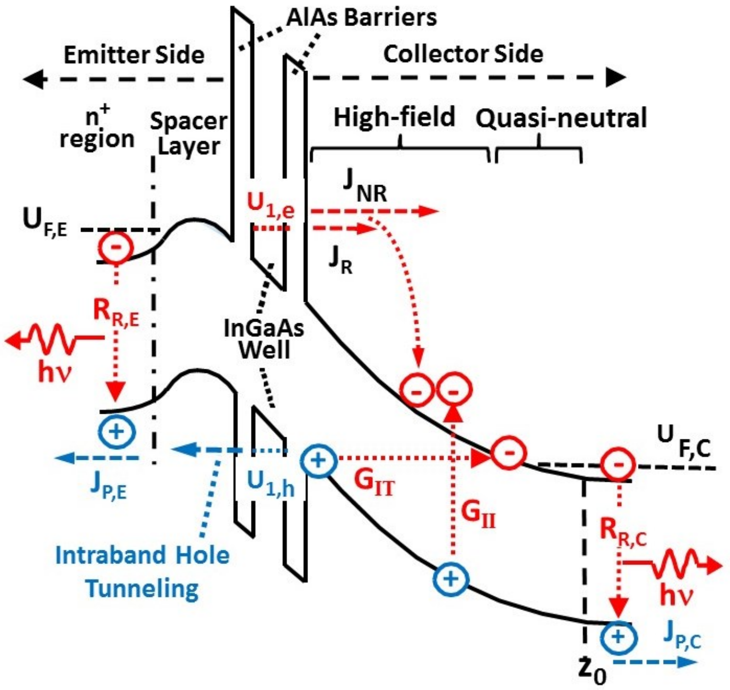

FIG. 6. Energy diagram showing a qualitative model for electron-hole generation by interband tunneling, G_{IT} , or by impact ionization, G_{II} , on the collector side of the $In_{0.53}Ga_{0.47}As$/AlAs RTD, and radiative recombination in either the emitter side, or in the quasi-neutral or n^+ regions on the collector side.

III.B. Independent Estimate of IQE

III.B.1. Electroluminescence Model

The experimental results and physical reasoning lead to a qualitative model for the high-bias electroluminescence, shown in the schematic diagram of Fig. 6, in which the charge transport is assumed to occur along the z axis. It assumes that electron-hole pairs are generated in the high electric-field ($E >> 0$) region on the collector side by either interband tunneling (G_{IT}) or impact ionization (G_{II}), with the total generation rate (number of holes per unit volume-time) represented by $G_{TOT} = G_{IT} + G_{II}$, both a function of z. Then the holes transport either to the emitter side by tunneling through the double-barrier structure, or to the quasi-neutral region ($E \approx 0$) of the collector side by diffusion. The former mechanism contributes to the an electric hole current density $J_{P,E}$, and the latter to $J_{P,C}$ After transport, the holes recombine with free electrons that are abundant in these regions because of the heavy n-type doping ($N_D = 2\times10^{18}$ cm^{-3}). The recombination is assumed to be either cross-gap radiative, represented in Fig. 6 by rates $R_{R,E}$ and $R_{R,C}$,or non-radiative defined by $R_{N,E}$ and $R_{N,C}$. Being a direct-band gap semiconductor, the InGaAs supports large R_R without involvement of phonons, and large R_N by Auger recombination in heavily-doped (n^+) regions. All of these mechanisms and assumptions are described further in Appendix A where they are used to support our charge-transport-based estimate of the light-emission performance.

Figure 6 displays qualitatively an important aspect of our structure, which is a non-uniform electric field across the high-field region on the collector side. This is caused by the n⁻ doping ($N_D = 1x10^{17}$ cm^{-3}) on this side, which is typically done in RTDs designed for electronic applications to reduce the voltage drop across the collector side without introducing deleterious scattering of tunneling electrons by ionized impurities. This is in contrast to the intrinsic condition typically practiced in Zener diodes and p-i-n impact-ionization devices. And it causes the electric field to be highest near the double-barrier structure on the collector side, and significantly smaller approaching the quasi-neutral region. As we will see further below, this tends to promote the strongest G_{IT} near the double barrier structure, and the strongest G_{II} near the quasi-neutral region where the kinetic energy of the electrons transmitted through the double-barrier structure is the highest. The transmission mechanism can be either by elastic resonant tunneling through the quasibound electron level $U_{1,e}$, and represented by J_R, or by inelastic tunneling through the double-barrier structure and represented by J_{NR}. Our model assumes that both can contribute to impact ionization in a manner that will be described below.

Another essential aspect of our model is the transport of holes once generated. Even though the high-field region on the collector side is n⁻ doped, it is mostly depleted of free electrons under high bias. Hence, the majority of holes should experience insignificant radiative and non-radiative recombination in the depletion region because of the sparsity of stationary free electrons there, and the low concentration of traps and recombination centers expected in high-quality epitaxial $In_{0.53}Ga_{0.47}As$. So the holes should either drift ("uphill" in Fig. 6) towards the double barrier structure, or diffuse ("downhill" in Fig. 6) towards the quasi-neutral region on the collector side. The drifting holes will encounter the double-barrier structure, which as we will discuss later, can support resonant-tunneling of holes as well as electrons. By contrast, the diffusing holes encounter no such barrier. The balance between drift and diffusion of the holes is an important and complicated aspect of our RTD light emitter, but we formulate the charge-transport analysis in such a way that we can extract the most important light-emission metric – the internal quantum efficiency (IQE) – without knowing this balance.

III.B.2. Charge-Transport Calculation

To obtain a charge-transport estimate of the IQE, we derive in Appendix A the following expression applicable to electroluminescence in any solid-state device:

$$IQE = \eta_r \cdot \eta_i = \eta_r\, e \cdot \Phi_{G,TOT} / J_T , \qquad (4)$$

where η_r is the radiative recombination factor and η_i is the electrical injection factor, $\Phi_{G,TOT}$ is the total *available* hole flux, and J_T is the terminal electrical current density. Since the radiometric approach to IQE does not have a direct dependence on charge transport, Eqn. (4) also serves as an independent test of

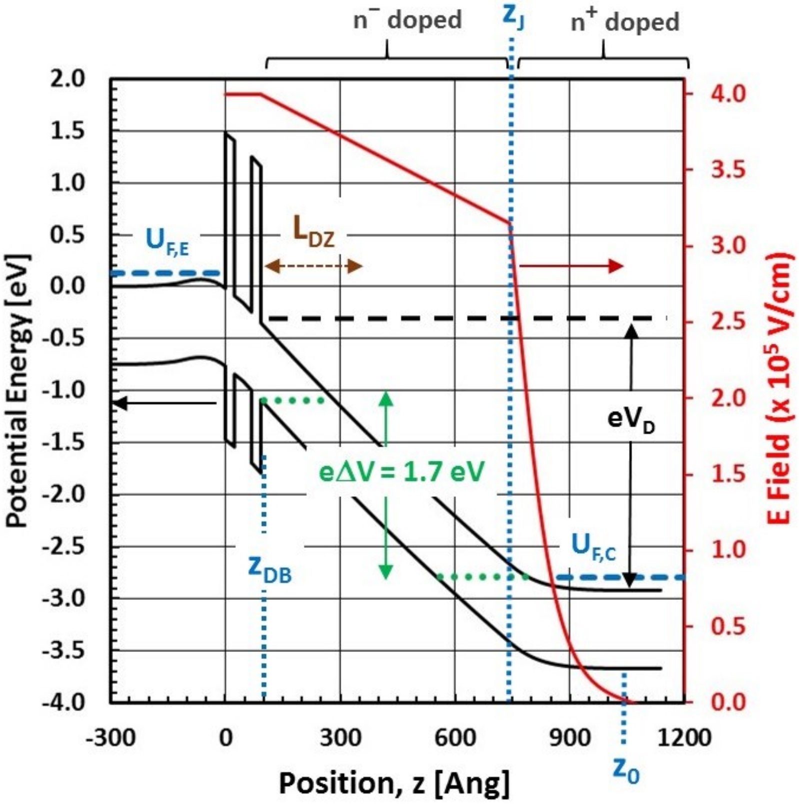

FIG. 7. Computed band bending (left vertical axis), and internal electric field (right vertical axis), for the qualitative models shown in Fig. 6 and a bias voltage of 2.9 V. Also shown is the energy range $\Delta E = e\Delta V$ ("tunneling window") over which interband tunneling can occur in the high-field region on the collector side.

our electroluminescence model of Fig. 6. Given the symmetric n^+ doping profile in the recombination regions, it is shown in Appendix A that

$$\eta_r = B\cdot n\cdot p/(B\cdot n\cdot p + C\cdot n^2\cdot p) = (1 + C\cdot n/B)^{-1} , \quad (5)$$

where B is the bimolecular recombination coefficient, and C is the three-particle (electron-electron-hole) Auger coefficient in these regions. In the n^+ regions, $n \approx N_D = 2\times10^{18}$ cm^{-3} for which $B \approx 1.4\times10^{-10}$ cm^3/s and $C \approx 8.1\times10^{-29}$ cm^6/s,[21] leading to $\eta_r \approx 0.46$. According to the model,

$$\Phi_{G,TOT} = \int_{z_{min}}^{z_{max}} (G_{IT} + G_{II})dz , \quad (6)$$

where G_{IT} is the generation rate associated with interband tunneling, G_{II} the generation rate by impact ionization, and z_{min} to z_{max} defines the range on the collector side where there is significant electron-hole generation. And as we will see below, both z_{min} and z_{max} depend on the mechanism.

For this analysis we first need an accurate evaluation of the band-bending in the device under bias. A representative plot of electron potential energy is shown in Fig. 7 at V_B = 2.9 V, derived from a numerical computation that connects a self-consistent Poisson-Schrödinger equation solver on the emitter side, to a Poisson solver on the collector side, both using the 2nd-order Unger approximation for the (degenerate) free electron density.[22] No accumulation of electrons is assumed to occur in the quantum well, which is a reasonable approximation when a double-barrier RTD is biased above the peak voltage at $V_B = 1.8$ V for the present device. Further aspects of the band bending and the associated internal electric field are described in Appendix B.

III.B.2.a. *Generation of Holes by Interband Tunneling*

To obtain the interband tunneling *available* hole flux $\Phi_{G,IT}$, we must apply an expression for G_{IT} and then integrate it across the high-field region being careful to only include z values that lie within the tunneling "window", i.e., connect a valence-band state to an unoccupied conduction band state at the same energy. Figure 7 depicts this tunneling window and the associated z locations at $V_B = 2.9$ V, z_{DB} being the collector-side edge of the double-barrier structure, and z_{max} being the furthest point in the high-field region where elastic tunneling can occur. Using the expression for G_{IT} described in Appendix C, we have:

$$\Phi_{G,IT} = \int_{z=z_{DB}}^{z_{max}} G_{IT} \cdot dz = \frac{2^{1/2}}{4\pi^3}\left(\frac{e}{\hbar}\right)^2 \left(\frac{m_r}{U_G}\right)^{1/2} \int_{z=z_{DB}}^{z_{max}} E^2(z) \cdot \exp\left[\frac{-\pi \cdot m_r^{1/2} \cdot U_G^{3/2}}{2^{3/2} e \cdot \hbar \cdot E(z)}\right] \cdot dz \qquad (7)$$

In our device at $V_B > \sim 1.0$ V, the tunneling window is approximately $\Delta V \approx V_C - (U_G - U_{F,C})/e$ where V_C is the voltage drop across the collector side and $U_{F,C}$ is the Fermi energy in the n^+ region on the collector side ($U_{F,C} \approx 0.131$ eV for $N_D = 2\times10^{18}$ cm^{-3} at 300 K). Then z_{max} is calculated from $z_{max} \approx z_{DB} + \Delta V/\overline{E}$ where $\overline{E} \equiv \int_{z_{DB}}^{z_0} E(z) \cdot dz$, the average across the high-field, n^-- doped region over which $|E| > 0$. For example, Fig. 7 shows that at $V_B = 2.9$ V, $V_C \approx 2.6$ V, $\Delta V = 1.7$ V, and $\overline{E} = 3.6 \times 10^5$ V/cm, so that $z_{max} = 56$ nm.

Given these conditions, we computed the available interband tunneling current, $e \cdot \Phi_{G,IT}$ from Eq. (7) and the corresponding band-bending diagram computed in steps of 0.1 V for V_B between 1.0 and 3.0 V. This included the additional relation $V_C = V_B - V_W - V_E$, where V_W and V_E are the voltage drops across the double-barrier structure and the emitter side, respectively. The resulting plot of $e \cdot \Phi_{G,IT}$ vs V_B is shown in Fig. 8, along with the light emission curve of Fig. 2 (right-hand axis of Fig. 8). The interband tunneling curve mimics the most important and practical aspect of the light emission behavior, which is the steep rise in photocurrent between ~2.5 and 3.0 V beyond the valley point. And in this same range of bias, the RTD

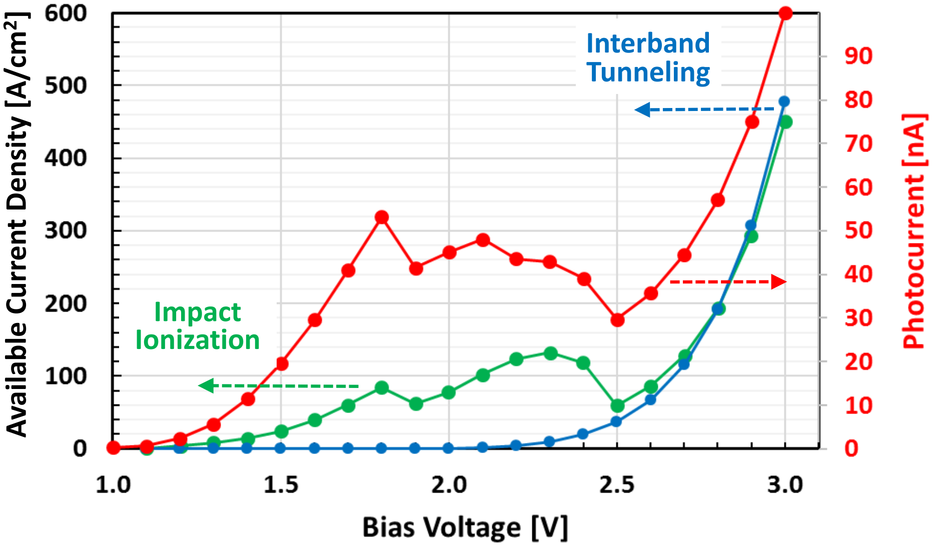

FIG. 8. Computed available current density for interband tunneling and impact ionization (left vertical axis) in comparison to photocurrent (right vertical axis). The interband tunneling curve assumes $U_G = 0.747$ eV and $m_r = 0.023\ m_e$. The impact ionization curve assumes electron ionization coefficients from Fig. 9.

electrical current is increasing much more slowly, suggesting that the light emission in this bias region is *field-driven* – consistent with interband tunneling, but perhaps impact ionization as well, as addressed next.

III.B.2.b. *Generation of Holes by Impact Ionization*

The other likely hole-generation mechanism in our device is impact ionization, which has been studied continuously in $In_{0.53}Ga_{0.47}As$ devices for several decades. Much of the interest has stemmed from making high-performance high-speed $In_{0.53}Ga_{0.47}As$ p-i-n photodiodes for 1550-nm fiber telecommunications, $In_{0.53}Ga_{0.47}As$ avalanche photodiodes for low-light sensing, or InP-based high-speed and low-noise transistors (HBTs and HEMTs) for analog and digital signal processing. As has been known

(a)

Region	E Range [x10^5 V/cm]	α(E)[1/cm]
I	< 1.5	$2.03\text{x}10^3 \cdot \exp[-(1.98\text{x}10^5/E)^{1.05}]$
II	1.5 – 2.3	$4.30\text{x}10^4 \cdot \exp[-(9.30\text{x}10^5/E)^{0.81}]$
III	2.3 – 3.0	$3.72\text{x}10^6 \cdot \exp[-(4.76\text{x}10^6/E)^{0.67}]$
IV (extrapolation)	> 3.0	$1.0\text{x}10^7 \cdot \exp[-(2.2\text{x}10^6/E)^{1.0}]$

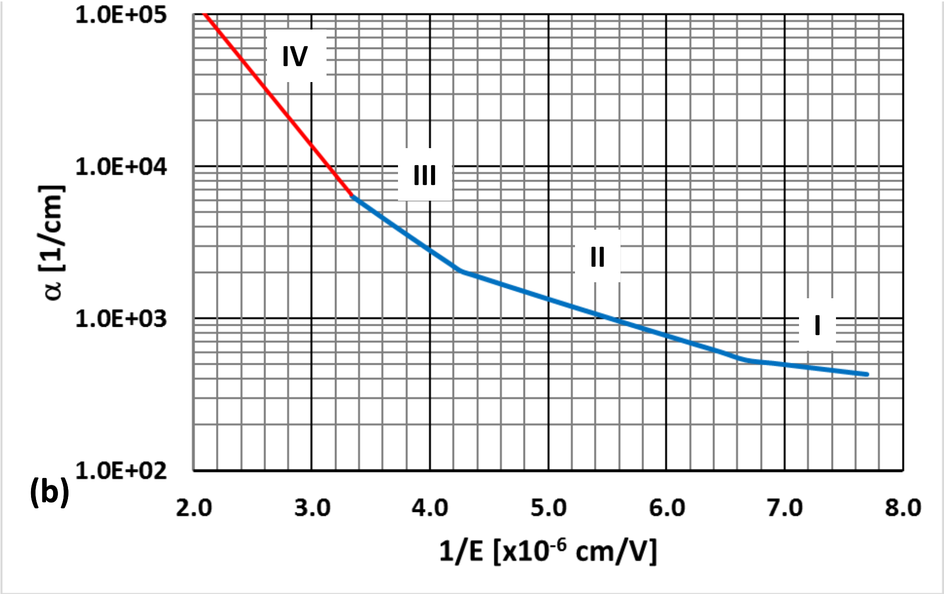

FIG. 9. (a) Table of expressions for electron impact ionization coefficient over four contiguous regions of internal electric field. (b) Graphical representation of (a).

since the early days of semiconductor devices, modeling impact ionization and distinguishing it from interband tunneling is tricky. Fortunately, the essential physical quantities to estimate the degree of hole generation – the electron and hole ionization coefficients defined here as α and β, respectively – have been derived by several researchers from both HBT and p-i-n photodiode measurements. Perhaps the most reliable method, involving calibrated photoexcitation of p-i-n photodiodes, has resulted in the threefold piecewise-continuous expressions for α tabulated in Fig. 9(a) and applicable at room temperature (300 K) up to an E field of 3×10^5 V/cm.[23] Above this value, we have carried out an extrapolation of region III up to E = 5×10^5 V/cm to define region IV, which is based on results from Monte-Carlo simulations.[24] This yields the traditional plot of α vs 1/E shown in Fig. 9(b). A similar curve can be constructed for β but in $In_{0.53}Ga_{0.47}As$ it is significantly smaller than α (e.g., $\alpha \approx 5\times\beta$ at E = 3×10^5 V/cm [Ref. 23]). Because the electrons comprising drift current across the depletion region of p-i-n photodiodes are generally thermalized (via phonon scattering), we expect these ionization coefficients to be applicable to the non-resonant tunneling electron current J_{NR} of Fig. 6, but perhaps underestimating the impact ionizing effect of elastic resonant tunneling current component J_R, as will be discussed further below.

Lacking p-doping, there should be a boundary in the biased structure of Fig. 7 beyond which the hole generation by impact ionization becomes negligible. For the present calculation, we assume this occurs in the collector-side n^+ region where the E field approaches zero, or at $z \equiv Z_0 \approx 105$ nm in Fig. 7 for 2.9 V bias. After drifting across the high-field region, electrons will relax very quickly because of the low field, and large free-electron and ionized-donor density beyond this boundary. Another important aspect is the inclusion of a "dead zone" starting at the double-barrier edge of the high-field region. This is where the kinetic energy of incoming electrons is below the threshold to induce an impact ionization event. Although the kinetic energy threshold U_{TH} is not well-defined in $In_{0.53}Ga_{0.47}As$ [Ref. 24], we can estimate it using the rule-of-thumb $U_{TH} = 1.5 \times U_G$ [Ref. 34] based on conservation of energy and momentum for electrons confined to parabolic conduction bands. This applies to $In_{0.53}Ga_{0.47}As$, at least for sufficiently low kinetic-energy electrons. Then given the band bending of Fig. 7, the "dead zone" length can be estimated as

$$L_{DZ} \approx 1.5 \cdot U_G / E_{MAX} \tag{8}$$

where E_{MAX} is the maximum electric field at the edge of the double-barrier structure, which is $\approx 4.0 \times 10^5$ V/cm at $V_B = 2.9$ V. This corresponds to $L_{DZ} \approx 28$ nm, and at lower bias, L_{DZ} will be even longer.

As with interband tunneling, we require an expression for the impact ionization available hole flux $\Phi_{G,II}$ obtained by integrating the generation rate G_{II} with respect to z. As derived in Appendix D, a simple but plausible approximation for G_{II} leads to

$$\Phi_{G,II} = \int_{z_{min}}^{z_{max}} G_{II} \cdot dz \approx (J_T/e) \cdot \int_{z_{DZ}}^{z_0} \alpha(z) \cdot dz \tag{9}$$

Using the piecewise-continuous expressions for $\alpha(E)$ in Fig. 9(a), this allows a numerical integration of Eqn. (9), which was carried out between $V_B = 1.0$ and 3.0 V in 0.1 V steps. The result is plotted in Fig. 8 as an *available* impact-ionization current in direct comparison with the interband-tunneling component. Clearly, the impact ionization current dominates at the lower bias voltages, but beyond the valley point becomes comparable to the interband current which rises faster with bias voltage. Nevertheless, both mechanisms mimic the behavior of the photocurrent in this bias region in that both rise much faster with bias than J_T, as shown clearly in Fig. 2. Hence, the impact ionization appears to be both *current* and *field driven*, the latter behavior arising from the strongly non-uniform behavior of α vs 1/E shown in Fig. 9(b).

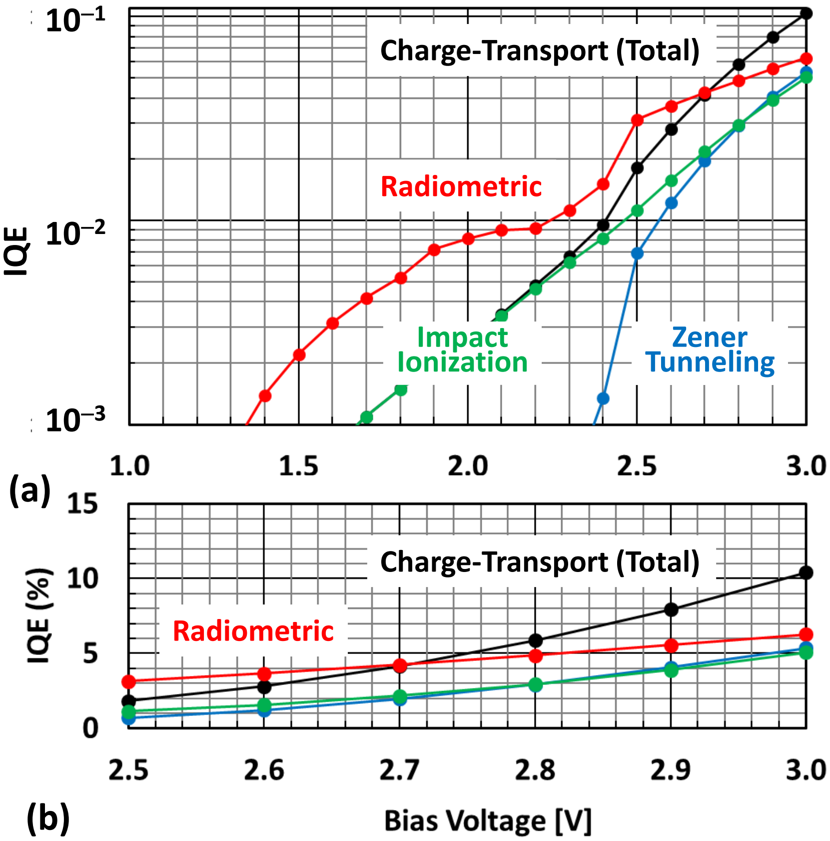

FIG. 10. (a). Internal quantum efficiency computed by the radiometric and charge-transport approaches, and showing the individual contributions by interband tunneling and impact ionization to the charge-transport approach. (b) Zoom-in on the high-bias region of (a) and plotted on a linear scale.

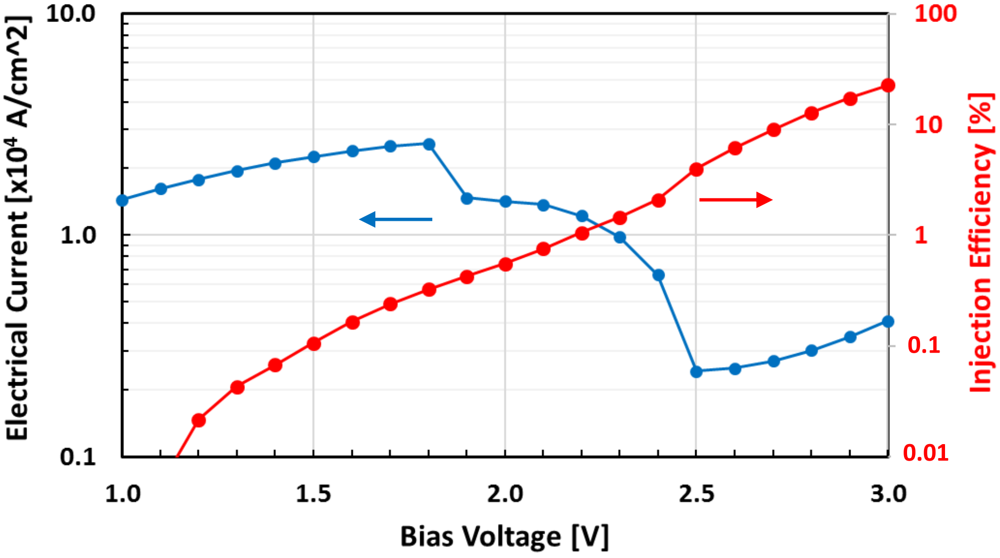

FIG. 11. Terminal electrical current (from Fig. 2) and available injection efficiency (right vertical axis).

III.B.2.c. Charge-Transport IQE vs Bias Voltage

Given the above analysis, we can construct the plot of Eqn. (4) vs V_B shown in Fig. 10(a) with the $e\Phi_{G,IT}$ and $e\Phi_{G,II}$ functions plotted individually and in total, along with the value $\eta_r \approx 0.46$ (from Eqn. 5) and the values of the terminal electric current density J_T from Fig. 2. Also displayed for comparison is the IQE curve for the radiometric calculation from Eq. (3) and Fig. 5. A zoom-in of the high-bias region beyond the valley point is shown in Fig. 10(b) where we see that at the highest bias voltage of 3.0 V, the charge-transport IQE is ≈10% compared to 6% for the radiometric approach. The discrepancy between the two decreases with reduced bias, so at $V_B = 2.7$ V they are practically equal, and below that the radiometric IQE exceeds the transport IQE by an amount that increases with decreasing bias.

A related plot and one that serves as a test of our modeling is shown in Fig. 11. It is the ratio $e\Phi_{G,TOT}/J_T = (e\Phi_{G,IT}$ and $e\Phi_{G,II})/J_T$, which from Eqn. 4 is the available injection efficiency η_i. We see that this increases very rapidly with bias voltage, consistent with the exponential nature of both the interband-tunneling and impact-ionization mechanisms. At the highest $V_B = 3.0$ V, it reaches ≈22%. Although not negligible as assumed in the development of Eqn. 9, it does support the statement that the generation of holes by impact ionization is primarily associated with the non-resonant electron current through the double-barrier structure (J_{NR} in Fig. 6) at bias voltages beyond the valley point.

IV. DISCUSSION

IV.A. Comparison of IQEs

In the bias region above the valley point, the radiometric and charge-transport IQEs agree favorably with the charge transport IQE increasing faster but equaling the radiometric value at 2.7 V, and exceeding it by only 67% at 3.0 V. This supports our transport model of Fig. 6 and suggests that both interband tunneling and impact ionization play a role in the hole generation necessary for the light emission. However, it has a more profound implication based on the fact that $e\Phi_{IT}$ and $e\Phi_{II}$ are only *available* current densities, not necessarily electrical current densities flowing in the recombination regions on the emitter or collector sides. So, the near equality of the IQEs suggests that the fraction of generated hole current that transfers to the recombination regions is large. For the diffusion process to the quasi-neutral region on the collector side, this is understandable since there is no barrier. However, at the high bias fields that exist above the valley point bias, we expect drift ("uphill") to be predominant over diffusion ("downhill), so the double-barrier structure serves as a bottleneck. Hence, the transfer efficiency of holes through the double-barrier structure must be significantly high. Being that holes have much poorer transport than electrons in $In_{0.53}Ga_{0.47}As$, this may be surprising. However, given the relatively narrow $In_{0.53}Ga_{0.47}As$ quantum well and the thin AlAs barriers, the hole quasibound states should be well defined such that hole resonant tunneling is likely. And as with electrons, the resulting net transmission is much larger than through a single barrier of comparable total thickness. Also the Γ-point barrier height for holes (≈0.7 eV) is considerably lower that for electrons (≈1.5 eV). And the spatial quantization splits the valence band degeneracy according to heavy-hole (m^*_{hh} = 0.46 m_e), and light-hole (m^*_{lh} = 0.052 m_e) masses, creating a multiply resonant transmission. These effects may collectively increase the average hole transmission, especially for light holes, to a comparable value as for electrons. And our preliminary computations of the zero-bias hole tunneling probability support this.

The difference in bias dependence of the two IQEs is also an important observation which we have considered but not yet fully analyzed. The $e\Phi_{G,IT}$ and $e\Phi_{G,II}$ *available* current densities of the charge-transport IQE are both strongly dependent on the band bending, as displayed in Fig. 7 at 2.9 V. However, this band bending profile does not account for hole accumulation in the high-field region on the collector side, especially accumulation of holes that are blocked by the double-barrier structure. This will tend to screen the electric field in this region, causing a more rapid fall with z than displayed by Fig. 7. This in turn will shrink the "window" for interband tunneling, and reduce the kinetic-energy increase of the electrons that drive the impact ionization. In either case, it will soften the dependence of the charge-transport IQE on bias voltage. It will also introduce a minority carrier diffusion capacitance, which must ultimately be understood to predict the speed capability of RTD light emitters.

The discrepancy between the radiometric and charge-transport IQEs in Fig. 10(a) at low bias (below the peak voltage of 1.8 V) is about a factor of four, meaning that our charge-transport model must be inaccurate in this region. In reports of light emission in n-GaAs RTDs, it was proposed that the elastic resonant-tunneling current (J_R in Fig. 6) is very efficient at generating impact ionization on the collector side because of its coherent, ballistic nature. While first observed at low temperature,[25] it has more recently been observed up to room temperature,[26,27] in all cases being attributed to impact ionization. This mechanism should also be present in our $In_{0.53}Ga_{0.47}As$ device, maybe even stronger than in GaAs because of the lower band gap and higher mobility in the $In_{0.53}Ga_{0.47}As$. Intuitively, its effect would be to increase the electron impact ionization coefficient α even higher than the values shown in Region IV of Fig. 9. However, the physical analysis so far has been based on the generalized Keldysh model with only qualitative fitting to the data, not the quantitative fitting made possible by impact ionization coefficients and followed in the present work. And none of these references have considered the interband-tunneling mechanism. Furthermore, since the light-emission performance is best in the bias region beyond the valley point where the α values of Fig. 9 should apply, we did not pursue this methodology in the present work.

IV.B. Design Issues

Finally, there is the open question of whether the RTD light emission performance can be made more efficient than the 6% IQE value reported here. Firstly, the double-barrier RTD structure should be made with a quantum well unusually narrow by RTD electronic-device standards. High-speed RTDs are generally designed with a quantum-well width having a ground-state energy $U_{1,e}$ ~100 meV. Combined with a n^--layer doping width of ~50 – 100 nm on the collector side, this usually yields a peak voltage of ~1.0 V and a high peak-to-valley ratio: 10 or higher in high-quality InGaAs/AlAs RTDs, and 3 or higher in high-quality GaAs/AlAs RTDs, both at room temperature. By contrast, RTD light emitters should be designed with narrower quantum wells to create $U_{1,e}$ approaching 200 meV or above, and peak voltages approaching 2.0 V, or above, assuming the PVCR remains high. This is because the electric field across the depleted region on the collector sides increases proportionate to the peak voltage, and both the interband tunneling and impact ionization mechanisms are exponentially dependent on the field, albeit in a complicated way.

The second issue is the length and doping concentration of the n^- layer on the collector side. Traditionally, these have been designed with respect to electrical capacitance and carrier transit time. If the n^- layer is too short (at the peak voltage), roughly 50 nm or less, there will be a significant space-charge capacitance under bias that can limit the speed of the device in electronic applications, such as THz oscillators and picosecond switches. Similarly, if the n^- layer is too long (at the peak voltage), roughly 100 nm or greater, there will be a significant transit-time delay that could also limit the speed in these applications. For RTD light emitters, at least LEDs, the speed will most likely be limited by the (natural) cross-gap radiative lifetime, of order 1 ns, although acceleration effects may be possible. Therefore to achieve higher IQE, it would be prudent to design the n^- region longer than in traditional RTDs, and doped to even lower levels, such as the “intrinsic” levels in p-i-n diodes. This will make the electric field more uniform and extended over a greater distance, to enhance both interband tunneling and impact ionization. Of course, this is a delicate business since both mechanisms can easily lead to device breakdown failure, the impact ionization hole generation increasing exponentially with length until avalanching occurs. However, provided breakdown is avoided and the RTD peak-to-valley current ratio remains high, the IQE in the valley region and somewhat beyond could readily exceed the 6% value reported here.

V. CONCLUSION

We have carried out spectral and radiometric measurements of the room-temperature electroluminescence from vertically emitting, unipolar n-doped $In_{0.53}Ga_{0.47}As$/AlAs RTDs. The emission occurs near the $In_{0.53}Ga_{0.47}As$ bandgap and has a peak wavelength consistent with an ideal electroluminescence behavior by spontaneous emission, and an intensity that increases rapidly with bias voltage beyond the valley point of the RTD. A model is presented that attributes the electroluminescence to electron-hole radiative recombination on the emitter side enabled by hole generation on the collector side and transfer to the emitter side. The EQE is rather low (2×10^{-5}) primarily because of the low optical coupling factor ($\eta_c = 3.4\times10^{-4}$); therefore, the radiometric IQE should be much larger and is found to be ≈ 6% at the highest V_B of 3.0 V. An independent charge-transport estimate of the IQE is obtained by separate computation of the available hole current density from the interband-tunneling and impact-ionization mechanisms. This required an accurate band bending profile, along with an assumption of Auger-limited non-radiative recombination on the emitter and collector sides. Altogether this enabled an independent estimate for IQE of ≈ 10% at $V_B = 3.0$ V. The closeness of the two IQEs suggests that the transport of holes out of the generation region and into the outlying recombination regions is effective, although the balance between recombination on the emitter and collector sides is not yet determined. Our results bode well for the potential application of this *unipolar-doped*, RTD-based emission technology in practical photonic source applications (e.g., LEDs), once improvements in the optical external coupling and hole generation mechanisms are fashioned through improvements in the device design.

ACKNOWLEDGMENTS

This work was supported by the U.S. National Science Foundation (under Grant #1711733). The authors thank Dr. Ravi Droopad for the MBE material growth.

DATA AVAILABILITY

The data that supports the findings of this study are available within the article

APPENDIX A

To obtain the charge-transport estimate of the IQE, we start with the fundamental definition applicable to electroluminescence in any vertically oriented solid-state device:

$$\mathrm{IQE} = \text{(internal photon-generation flux) /(total charge-carrier flux)} \equiv \Phi_{R,R}/\Phi_Q \qquad (A.1)$$

where flux has the usually meaning in transport theory (number per unit area·time) and applies here assuming all transport mechanisms are uniform across any horizontal plane perpendicular to the electric current flow. For the model of Fig. 6, the internal radiative-recombination flux is just

$$\Phi_{R,R} = \int_E R_R(z)dz + \int_C R_R(z)dz \qquad (A.2)$$

$R_R(z)$ is the spontaneous radiative recombination rate of electron-hole pairs (i.e., "bimolecular"), and E and C denote the emitter and collector sides of the structure, respectively, and. The integrals are assumed to span far enough along the z axis of the emitter and collector sides to account for all radiative recombination from the device. The total charge-carrier flux is just the terminal current density J_T per unit charge, $\Phi_Q = J_T/e$, where J_T for the present device is plotted in Fig. 2. This leads to the compact expression

$$\mathrm{IQE} = e\cdot\Phi_{R,R}/J_T \qquad (A.3)$$

In competition with the radiative mechanism of Eqn (A.2) is the non-radiative recombination for which we can write another flux

$$\Phi_{R,N} = \int_E R_N(z)dz + \int_C R_N(z)dz \qquad (A.4)$$

where again, the integrals are assume to span far enough along z to account for all of the non-radiative recombination. This leads to a total recombination flux

$$\Phi_{R,TOT} = \Phi_{R,R} + \Phi_{R,N} \qquad (A.5)$$

To proceed further, relationships are needed between $\Phi_{R,TOT}$, $\Phi_{R,R}$, and $\Phi_{R,N}$. According to the model in Fig. 6, all recombination occurs in the n^+ regions on the emitter side, and in the quasi-neutral region or beyond on the collector side. For direct-bandgap semiconductors like $In_{0.53}Ga_{0.47}As$, rate-equation analysis commonly used in LED and laser-diode devices defines a (spontaneous) radiative recombination rate of

$$R_R(z)= B\cdot n\cdot p \qquad (A.6)$$

where B is the bimolecular recombination coefficient, and n and p are the local electron and hole densities, respectively. In principle, all three of these quantities depend on z. Assuming n >> p, the non-radiative recombination rate can be estimated through the Auger recombination expression involving three electrons and one hole (often called CCCH, CHCC, or Auger process #1 in the literature):

$$R_N(z) = C\cdot n^2\cdot p, \qquad (A.7)$$

where C is the associated Auger coefficient. As in Eqn (A.6), C, n, and B are inherently functions of z. This leads to a useful expression for the ratio of $\Phi_{R,R}$ to $\Phi_{R,TOT}$

$$\frac{\Phi_{R,R}}{\Phi_{R,TOT}} = \frac{\int_E \mathrm{B\,n\,p\,dz} + \int_C \mathrm{B\,n\,p\,dz}}{\int_E (\mathrm{B\,n\,p} + \mathrm{C}\,n^2\mathrm{p})\mathrm{dz} + \int_C (\mathrm{B\,n\,p} + \mathrm{C}\,n^2\mathrm{p})\,\mathrm{dz}} \equiv \eta_R \qquad \text{(A.8)}$$

And we can re-write the IQE from Eqn. A.3 compactly as

$$\mathrm{IQE} = e\cdot\eta_R\,\Phi_{R,TOT} / J_T \qquad \text{(A.9)}$$

where η_R is the radiative recombination factor. If we now assume that n(z) on both the emitter and collector sides is uniform and equal to the local n^+ donor density N_D, then B and C will also be uniform on each respective side and we can write

$$\eta_R = \frac{(BN_D)_E \int_E p(z)dz + (BN_D)_C \int_C p(z)\,dz}{(BN_D + CN_D^2)_E \int_E p(z)dz + (BN_D + CN_D^2)_C \int_C p(z)\,dz} \qquad \text{(A.10)}$$

While in general requiring knowledge of the hole spatial density on each side, it has a great simplification in a symmetrically doped structure where N_D is the same on both sides, leading to

$$\eta_R = \frac{BN_D\left[\int_E p(z)dz + \int_C p(z)\,dz\right]}{(BN_D + CN_D^2)\left[\int_E p(z)dz + \int_C p(z)\,dz\right]} = \frac{BN_D}{BN_D + CN_D^2} = \frac{1}{1 + CN_D/B} \qquad \text{(A.11)}$$

by cancellation of the hole spatial integrals.

Lastly, according to our model, all of the holes are assumed to be generated in the E > 0 region on the collector side and associated with a total generation rate G_{TOT}, and associated flux

$$\Phi_{G,TOT} = \int_{E>0} G_{TOT}\cdot dz \qquad \text{(A.12)}$$

In steady state, *the total recombination flux must equal the total generation rate*, $\Phi_{R,TOT} = \Phi_{G,TOT}$. Hence we can re-write the IQE as

$$\mathrm{IQE} = e\cdot\eta_R\,\Phi_{G,TOT} / J_T \equiv \eta_R \cdot \eta_I \qquad \text{(A.13)}$$

where η_I is the so-called electrical injection efficiency. And remarkably, this expression does not require knowledge of the hole densities in either recombination region.

APPENDIX B

The band-bending plot of Fig. 7 shows that as might be expected, the majority of bias voltage drops across the collector side, creating a high-field region that extends over the entire 65-nm n-doped ($N_D = 1x10^{17}$ cm^{-3}) on this side, and partially into the n^+-doped region outside it. It also shows the magnitude of the internal electric field E(z) obtained from $E(z) = |d\phi/dz|$, where ϕ is the electrostatic potential. E(z) is the most important physical quantity in interband tunneling and is similarly important for impact ionization. In the present structure, E has a maximum value, E_{max}, at the boundary between the double-barrier structure and the n-doped region, which remains true even if there is some electron accumulation in the quantum well. On the collector side, E(z) decreases gradually across the low-doped region and then rapidly at the n^- - n^+ homojunction shown at $z = z_J$ in Fig. 7. It then falls to zero at $z = z_0$, which occurs ≈30 nm beyond z_J at 2.9-V, but less beyond z_J at lower bias. The small drop in E of only ~25% across the n^--doped region is important since this helps justify the transport analysis given below.

We note that the AlAs barriers are assumed to present an electron barrier height of $\phi_{B,e} = 0.68\cdot\{E_G(AlAs) - E_G(InGaAs)\} = 1.50$ eV, and a hole-barrier height of $\phi_{B,h} = 0.32\cdot\{E_G(AlAs) - E_G(InGaAs)\} = 0.70$ eV , where E_G (AlAs) is the room-temperature band gap (≈2.95 eV) of AlAs at the Γ point,[28] and E_G (InGaAs) is the bandgap of $In_{0.53}Ga_{0.47}As$ (≈0.75 eV) at the same point.[29] This is the same band offset as for the lattice-matched $In_{0.53}Ga_{0.47}As/In_{0.52}Al_{0.48}As$ Type-I heterojunction.[30] However, it ignores the lateral tensile strain that the thin AlAs barriers undergo when embedded in $In_{0.53}Ga_{0.47}As$ – an issue still not fully resolved after 30 years of successful application.

APPENDIX C

Following Zener's seminal paper, more detailed theoretical work on interband tunneling was carried out in the 1950s and 60s first by Keldysh,[31] and then by Kane.[32, 33] Kane's second paper focused on the general case of interband tunneling across the junction of heavily-doped p-n junctions. Here we apply a simplification of this analysis described succinctly by J. Moll and applied to the interband tunneling case between a fully occupied valence and an empty conduction bands under the influence of a large internal electric field.[34] For direct, narrow-bandgap semiconductors like $In_{0.53}Ga_{0.47}As$, this process is expected to be elastic meaning that phonons are not necessary. In analyzing the interband current density across the intrinsic (i) region of a back-biased p-i-n junction, Moll derived an expression for the terminal current that does not apply exactly to our device because of our non-uniform field and the blocking effect of the double-barrier structure. However, it corresponds to the following approximate local generation rate in the high-field region:

$$G_{IT}(z) \approx \frac{2^{1/2}}{4\pi^3}\left(\frac{e}{\hbar}\right)^2 \cdot E^2(z) \cdot \left(\frac{m_r}{U_G}\right)^{1/2} \cdot \exp\left[\frac{-\pi \cdot m_r^{1/2} \cdot U_G^{3/2}}{2^{3/2} e \cdot \hbar \cdot E(z)}\right] \tag{C.1}$$

where E(z) is the local electric field, m_r is the reduced effective-mass, and U_G is the band gap energy. The reduced mass is given by $m_r = (1/m_c + 1/m_v)^{-1}$ where m_c and m_v are the electron and light-hole masses, respectively. This definition is best suited to narrow-band-gap III-V semiconductors like InSb and InAs, but should be a good approximation for $In_{0.53}Ga_{0.47}As$. The strongest effect on G_{IT} occurs through the $U_G^{3/2}$ and E^{-1} terms in the argument of the exponent. For $In_{0.53}Ga_{0.47}As$, we use the room-temperature values $U_G = 0.747$ eV, $m_c = 0.042\ m_e$, and $m_v = m_{lh} = 0.051\ m_e$, so that $m_r = 0.023\ m_e$.[35]

APPENDIX D

For semiconductors there exists the following general expression for the local, *current-driven*, impact-ionization generation rate (Ref 34):

$$G_{II}(z) = (1/e)\ [\alpha(z)\cdot J_N(z) + \beta(z)\cdot J_P(z)] = (1/e)\ dJ_{II}/dz \tag{D.1}$$

where α and β are the electron and hole impact ionization coefficients, J_N and J_P are the *net* electron and hole electrical current densities, and J_{II} is the *available* hole current corresponding to G_{II} . J_N includes contributions from the electron resonant-tunneling current J_{RT} the interband-tunneling current J_{IT} and the impact ionization currents J_{II}, such that $J_N = J_{RT} + J_{IT} + J_{II}$, whereas J_P includes contributions only from the J_{IT} and J_{II}. It is understood that Eqn. (D.1) changes with each bias voltage and thus each electric-field distribution across the device. However, independent of bias, the steady-state current-continuity relation, $J_N(z) + J_P(z) = J_T$ (a constant), must apply at all z. Hence, we can re-write (D.1) as

$$G_{II}(z) = (1/e)\{\alpha(z)\cdot J_T + [\beta(z) - \alpha(z)]\cdot J_P(z)\} \tag{D.2}$$

This re-arrangement is motived by the fact that J_T is a known quantity – the total (terminal) electrical current density plotted in Fig. 2 for our particular device. An analytic solution to Eqn. (D.2) is complicated by the fact that $J_P(z)$ includes both the interband-tunneling and impact-ionization mechanisms, which have different spatial dependencies in our structure as discussed above for our electroluminescence model of Fig. 6. The interband mechanism should generate the most holes between $z = z_{DB}$ and $z \approx z_J$, where, as shown in Fig. 7, the E field is the strongest. The impact ionization should generate the most holes between $z = z_{DZ}$ and z_0 where the electrons should have their highest kinetic energy. To alleviate this complexity, we take advantage of the simplification that occurs when the 2nd term of (D.2) is negligible compared to the first term. This happens naturally when $\alpha(z) \approx \beta(z)$ as occurs in semiconductors like GaAs and Si at high fields. But as described above, this it is not so true in $In_{0.53}Ga_{0.47}As$. So instead, we assume simply that $J_P(z)$ is << J_T at all z, which allows us to immediately write from Eqn (D.2),

$$G_{II} \approx (J_T/e)\ \alpha(z) \tag{D.3}$$

REFERENCES

---

[1] C. Zener, Proc. Royal Society **145**, 523 (1934).

[2] L. Esaki, Phys. Rev. **109**, 603 (1958).

[3] W. Hansch, C. Fink, J. Schulze, I. Eisele, Thin Solid Films **369**, 387 (2000).

[4] P.M. Solomon, J. Jopling, D. J. Frank, C. D'Emic, O. Dokumaci, P. Ronsheim, and W. E.Haensch, , J. Appl. Phys. **95**, 5800 (2004).

[5] A.C. Seabaugh and Q. Zhang, Proc. IEEE **98**, 2095 (2010).

[6] G. Dewey, B. Chu-Kung, R. Kotlyar, M. Metz, N. Mukherjee, and M. Radosavljevic,, in Symposium on VLSI Technology Digest of Technical Papers (2012), pp. 45-46.

[7] J.N. Schulman and D.H Chow IEEE Electron Device Letters 21 , 353 (2000)

[8] R. R. King, D. C. Law, K. M. Edmondson, C. M. Fetzer, G. S. Kinsey, H. Yoon, R. A. Sherif, and N. H. Karam, Appl. Phys. Lett. **90**, 183516 (2007).

[9] H.I. Cantu, B. Romeira, A.E. Kelly, C.N. Ironside, and J.M.L. Figueiredo, IEEE Trans Microwave Theory Tech. **60**, 2903 (2012).

[10] R.M. Lewis, H.P. Wei, S.Y. Lin, and J.F. Klem, Appl. Phys. Lett. 77, 2722 (2000),

[11] T.A. Growden, W. Zhang, E. R. Brown, D. F. Storm, D. J. Meyer, and P. R. Berger, Nature Light: Science & Applications **7**, 17150 (2018).

[12] E. R. Brown, W-D. Zhang, T. A. Growden, P. R. Berger, R. Droopad, arXiv 1804.07666 (2018).

[13] M. Feiginov C. Sydlo, O. Cojocari, and P. Meissner, Appl. Phys. Lett., 99, 233506 (2011).

[14] E. R. Brown E.R. Brown, J.R. Söderström, C.D. Parker, L.J. Mahoney, K.M. Molvar, and T.C. McGill, Appl. Phys. Lett. **58**, 2291 (1991).

[15] Stellarnet, Inc. "DWARF-Star" NIR spectrometer; www.stellarnet.us

[16] D.K. Gaskill and N. Bottka, Appl. Phys. Lett. **56**, 1269 (1990).

[17] E.F. Schubert, in *Light-Emitting Diodes*, 2nd Ed. (Cambridge Univ. Press, Cambridge, 2006).

[18] www.thorlabs.com: LED partnumbers 1600L and 1600P.

[19] I. Moreno and C.C. Sun, Optics Express **16** (3), 1808 (2008).

[20] E. R. Brown, W. Zhang, P. Fakhimi, T. A. Growden and P. R. Berger, in Proceedings of the 2020 Device Research Conference (DRC), pp. 1-2; doi: 10.1109/DRC50226.2020.9135175

[21] R. K. Ahrenkiel, R. Ellingson, S. Johnston, and M. Wanlass, 72 (26), 3470 (1998).

[22] K. Unger, Phys. Stat Solidi(b) **149**, K141 (1988).

[23] J.S. Ng, C.H. Tan, J.P.R. David, G. Hill, and G.J. Rees, IEEE Trans. Electron Dev. **50**, 901 (2003).

---

[24] J. Bude and K. Hess, J. Appl. Phys. 72, 3554 (1992)

[25] C.R.H. White, M.S. Skolnick, L Eaves, and M.L. Leadbeater, Appl. Phys. Lett., **58**, 1164 (1991).

[26] F. Hartmann, A. Pfenning, M. Rebello Sousa Dias, F. Langer, S. Höfling, M. Kamp, L. Worschech, L. K. Castelano, G. E. Marques, and V. Lopez-Richard, J. Appl. Phys. **122**, 154502 (2017).

[27] C. de Oliveira, A. Pfenning, E. D. Guarin, M. D. Teodoro,, E. C. dos Santos, V. Lopez-Richard, G. E. Marques, L. Worschech, F. Hartmann, and S. Höfling, Phys. Rev. B **98**, 075302 (2018).

[28] S. Adachi, *Physical Properties of III-V Semiconductor Compounds* (John Wiley, New York, 1992).

[29] Note that although AlAs is an indirect-gap semiconductor, the barriers are assumed so thin that a Γ-pt electron or hole from the InGaAs is assumed to remain in Γ valley of the AlAs during tunneling since this is consistent with the conservation of lateral crystal momentum.

[30] W.R. Frensley, in *Heterostructure and Quantum Devices*, ed. by N. G. Einspruch and W. R. Frensley, (Academic, Orlando, 1994).

[31] L.V. Keldysh, Soviet Phys. JETP **34**, 665 (1958).

[32] E.O. Kane, J. Phys. Chem. Solids **12**, 181 (1959).

[33] E.O. Kane, J. Appl. Phys. **32, 83** (1961).

[34] J. Moll, *Physics of Semiconductors,* (McGraw-Hill, New York, 1964).

[35] Yu A Goldberg & N. M. Schmidt, in *Handbook Series on Semiconductor Parameters; vol. 2: Ternary And Quaternary III-V Compounds*, ed. by M. Levinshtein, S. Rumyantsev, and M. Shur (World Scientific, 1996).